




Research Article

Similar Simulation Test on Deformation Characteristics of Overlying Rock Developed by Instability of Strip Coal Pillar

Yong Liu ^{1,2}, Bing Chen ³, Shilei Cui,¹ and Dawei Yin ³

¹Shangwan Coal Mine of Shendong Coal Group, Mongolia 017200, China

²General Control Room of National Energy Investment Group Co., Ltd, Beijing 100010, China

³State Key Laboratory of Mining Disaster Prevention and Control Co-Founded, Shandong University of Science and Technology, Qingdao 266590, China

Correspondence should be addressed to Bing Chen; cb2kw@sdust.edu.cn

Received 10 June 2022; Revised 12 July 2022; Accepted 14 July 2022; Published 8 August 2022

Academic Editor: Tao Meng

Copyright © 2022 Yong Liu et al. This is an open access article distributed under the Creative Commons Attribution License, which permits unrestricted use, distribution, and reproduction in any medium, provided the original work is properly cited.

In order to protect surface buildings and maximize the recovery of coal resources, there are a large number of strip coal pillars and unfilled goafs left in strip mining areas in China. Affected by the comprehensive factors such as long-term overlying rock load, water accumulation in goafs, and adjacent mining, the instability probability of strip coal pillar increases greatly, which becomes a potential hidden danger of surface disaster. However, the law of overlying rock and surface movement caused by strip coal pillar instability is not clear up to now. Therefore, a series of experimental studies on the law of overlying rock movement and deformation induced by strip coal pillar instability are carried out in this paper. The results show that it is feasible to use paraffin-containing materials to make a strip coal pillar model and simulate strip coal pillar instability by heating paraffin. After mining, the subsidence curve of the L5 monitoring line and its upper strata is “disk.” After the instability of the strip coal pillar, the subsidence curve changes from “disk” to “basin.” The instability of strip coal pillar can lead to significant and more harmful overburden movement between overburden and surface than that of strip working face. However, because the unstable coal pillar still has a certain bearing capacity, the maximum subsidence of the surface is still far less than that under the condition of longwall mining.

1. Introduction

Strip mining is a comprehensive subsidence reduction technology. It is widely used in our country. The test and practice of strip mining of pressed coal below hundreds of buildings have been carried out in more than ten mining areas, such as in Fushun, Fuxin, Jiaohe, Fengfeng, Hebi, Pingdingshan, Xuzhou, and so on [1–5]. Good results have been achieved in controlling surface subsidence and protecting ground buildings [6–10].

Whether the strip coal pillar can maintain long-term stability is the key to the success of strip mining. Scholars at home and abroad have done a lot of research on the stability of strip coal pillar, mainly focusing on the overlying load of coal pillar and its own strength, the design of mining width and retention width of strip mining, the analysis and evaluation of coal pillar stability, and so on. Snodgrass and

Newman [11] used the borehole acoustic detection method to determine the stability and plastic failure zone of coal pillar. Khai and Peng [12] found that when the bending degree of the roof exceeds its deflection limit, the accumulated elastic energy can be suddenly released to cause continuous instability of the coal pillar. Lu [13] evaluates the stability of coal pillar in the mining process by means of field and indoor triaxial tests. Based on the analysis of coal pillar strength, Salamon and Munro [14] derived the calculation formula for the safety factor of weak plane shear strength in any direction. Hu [15] proposed that the failure and instability of coal pillar is a typical nonlinear process. Xie et al. [16] obtained the stress expression of strip coal pillar in inclined coal seam with the help of the analysis principle of subordinate area method. Cui and Miu [17] analyzed the influence of dip angle on coal pillar stability by limit equilibrium method. Gao [18] analyzed the stability of strip

coal pillar by using fuzzy mathematics theory. Guo et al. [19] analyzed the width of yield zone of strip coal pillar and its influencing factors and put forward the limit equilibrium theory of the yield zone of strip coal pillar and the variation law and calculation method of yield zone width of strip coal pillar. Through the study of long-term stability monitoring and numerical simulation of strip coal pillar, Yang et al. [20] found that strip coal pillar showed obvious creep characteristics under long-term load. Chen [21] designed creep tests of coal samples with different water content. It is concluded that water content has an obvious effect on the creep characteristics of coal samples. The creep strength of coal samples increases with the increase of water content. According to the field measured results, Guo et al. [22] concluded that the width of the plastic zone of strip coal pillar in the deep roadway increased obviously, and the surface deformation of the multistrip mining area was continuous and longterm.

Although scholars at home and abroad have made rich achievements on the stability of strip coal pillar [23–25], there are few reports on the surface subsidence developed by the failure of overlying rock structures caused by the instability of strip coal pillar. The relationship between strip coal pillar instability, overlying rock failure and deformation, and surface disasters is not clear. For this reason, this paper studied the deformation law and failure characteristics from overlying rock to the surface caused by coal pillar and coal pillar group instability by means of physical similarity simulation. The research results have important guiding significance for the prevention and control of surface subsidence caused by strip coal pillar instability.

2. Engineering Background and Scheme Design

2.1. Geological Conditions. In this experiment, the northern part of the third mining area of a mine in Shandong Province is taken as the geological prototype, and the specific location distribution is shown in Figure 1. The ground elevation in the area is +36.1–+43.5 m. The floor elevation of coal seam 3 is –250.0~–320.0 m, the average thickness of the coal seam is 6 m, and the average buried depth is about 338.42 m. As there are two villages on the surface, strip mining is used to protect the surface villages from damage.

The test model of similar materials is established based on the stratigraphic distribution in the geological prototype area. Due to the limitations of test conditions, the strata need to be reasonably simplified and adjusted. The simplified geological prototype consists of upper, middle, and lower quaternary formations and Permian Shanxi formation from top to bottom, in which the quaternary loose layer is mainly composed of coarse sand clay (subclay) interbed, the roof bedrock is dominated by sandstone and local mudstone, the floor is dominated by medium-grained sandstone, and the direct floor is mudstone, as shown in Figure 2.

2.2. Test Scheme Design

2.2.1. Material Selection and Proportioning of Strip Coal Pillar. The temperature-controlled strip coal pillar model was prefabricated with river sand, paraffin, and hydraulic oil.

The selected river sand, paraffin, and hydraulic oil were used as raw materials to prepare the strip coal pillar model with the ratio of river sand: paraffin: hydraulic oil = 1500:100:100. The electric heating wire is embedded in the model, the electric heating wire voltage is controlled to soften the paraffin wax step by step, the heating process is well controlled, and then the coal pillar strength is reduced to the instability process simulation.

In order to verify that the model material selected in this paper meets the conditions of uniformity and stability, standard cylindrical samples with a size of 50 × 100 mm are made, and the finished standard samples are shown in Figure 3. Before the test, standard samples are weighed, the height and diameter are measured, the density is calculated, parameters of samples and the calculation results are shown in Table 1.

The uniaxial compression test of standard samples [26–32] was carried out by using the Shimadzu rock mechanics testing machine. The test process adopted the displacement control mode at a rate of 0.01 mm/s [29, 33–35]. The stress-strain curves obtained from the test are shown in Figure 3.

By analyzing the results of the uniaxial compression test, it can be concluded that the strength dispersion of similar materials under this ratio is small, which meets the requirements of a similar simulation test for uniform and stable material properties.

2.2.2. Selection and Proportion of Overburden Materials.

The cementing materials selected in this simulation test are gypsum and light calcium carbonate, and the selected aggregate is natural river sand. In order to ensure the homogeneity of the similar model, the larger sand particles in the river sand were screened before the experiment, and the water in the river sand was dried to ensure the accuracy of water consumption. According to the mechanical properties of each rock layer in the stratigraphic prototype, the appropriate proportion is selected, and equation (1) is used to calculate the amount of each layer material in the model, respectively. The results are shown in Table 2.

$$G = lbh\gamma_m, \quad (1)$$

where G —Model delamination material quality; l —Model length, m ; b —Model width, m ; h —Thickness of each layer in the model, m ; γ_m —The bulk density of each layer in the model, kg/m^3 .

2.2.3. Test Model Laying Process. The prefabricated coal pillar is 40 cm × 20 cm × 4 cm according to the width of the similar material test-bed and the size of the mould. 40 cm is the width of a two-dimensional similar material simulation test-bed, 20 cm is the designed width of a temperature-controlled strip coal pillar, and 4 cm is the thickness of coal seam. Each prefabricated coal pillar is uniformly distributed with 6 m long Ni–Cr alloy electric wire, the resistance of each electric wire is 102 Ω, the exposed length of the electric wire is the same, and the laying state of the temperature-controlled strip coal pillar is shown in Figure 4.

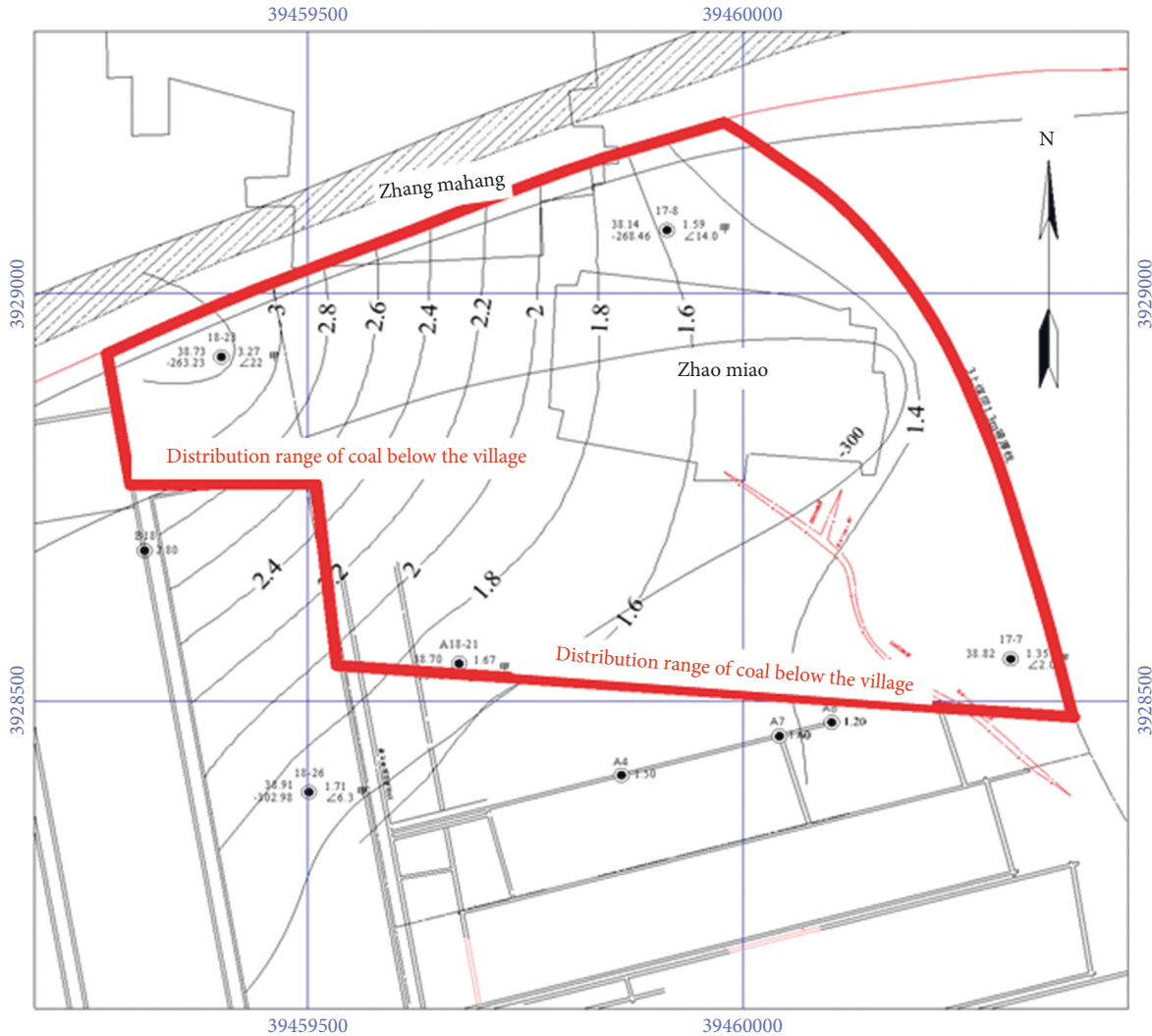


FIGURE 1: Similar simulated geological prototype area (Red line in the figure).

According to the properties and structural characteristics of the coal seam roof and floor in the project site, a total of 30 strata are laid in this similar simulation, and the layers are distinguished by mica powder. The dip angle of a coal seam in the field is small, so in order to facilitate the study, the dip angle of the coal seam is set to 0° in this paper. The overall size of the test model is $3000\text{ mm} \times 400\text{ mm} \times 1370\text{ mm}$ (length \times width \times height). The length and width are equivalent to 450 m in dip length and 60 m in strike length, respectively. Iron blocks are used to compensate for the weight of unladen strata.

2.2.4. Surface Displacement Monitoring Point Setting. A total of 9 horizontal grid lines and 29 longitudinal grid lines are arranged on the model's surface with ink lines by a spacing of 10 cm. At the same time, a pin is used to fix the reflector as the displacement observation point at the grid intersection, and the pin is located at the center of the circle. The surface displacement measuring line is arranged as shown in Figure 5.

3. Test Results

3.1. During Working Face Mining. In this experiment, a total of 7 working faces were designed, which were named "1# working face", "2# working face", "3# working face", "4# working face", "5# working face", "6# working face," and "7# working face" according to the mining direction. Design 6 strip coal pillars, which are named coal pillars and coal pillars in turn according to the mining direction. The east side of the border protection pillar is the 1# protective coal pillar, and the west side is the 2# protective coal pillar. The strip working face is mined in the order from east to west, and the mining process is shown in Figure 6.

After mining the working face, the direct roof falls immediately, and the falling height of each working face is basically the same. Because there are strata with large thickness and good lithology in the roof, the development of fracture zone and bending subsidence zone is not obvious in the process of simulation. This phenomenon is consistent with the movement and deformation law of overlying rock when the actual strip is opened. The falling height of the first



Stratigraphic system	1:500	Lithologic characteristics
Shanxi formation		<p>It is composed of siltstone, mudstone, fine grained sandstone and coal seam. The upper part is mainly mudstone, siltstone, local medium sandstone. The middle and lower part is mainly composed of medium sandstone and fine sandstone. The bottom of sandstones are characterized by the siltstones with benthic channels, and belong to transitional facies deposits.</p> <p>There are 4 layers of coal (2 coal, 3_{u1} coal, 3_u coal and 3_d coal), it is the main coal bearing stratum in the mine field. 3_{u1} coal seam is the main mining seam with a relatively stable thickness of 3.8~9.60 m and gradually thickening from north to south with an average of 5.85 m.</p> <p>The medium and fine grained sandstone in the 3_u coal roof, 3_d coal roof and 3_d coal floor are semi-sealed weak water-rich fractured confined aquifers with static reserves.</p>
Taiyuan formation		<p>The Carboniferous Taiyuan Formation, with thickness of 144.9~183.1 m and the average thickness of 170.0 m, it is composed of siltstone, mudstone, quartzite and coal seam.</p> <p>Taiyuan Formation is mainly composed of watertight mudstone, siltstone and fine sandstone, it has great influence on water filling of ore deposit.</p>

FIGURE 2: Stratigraph.

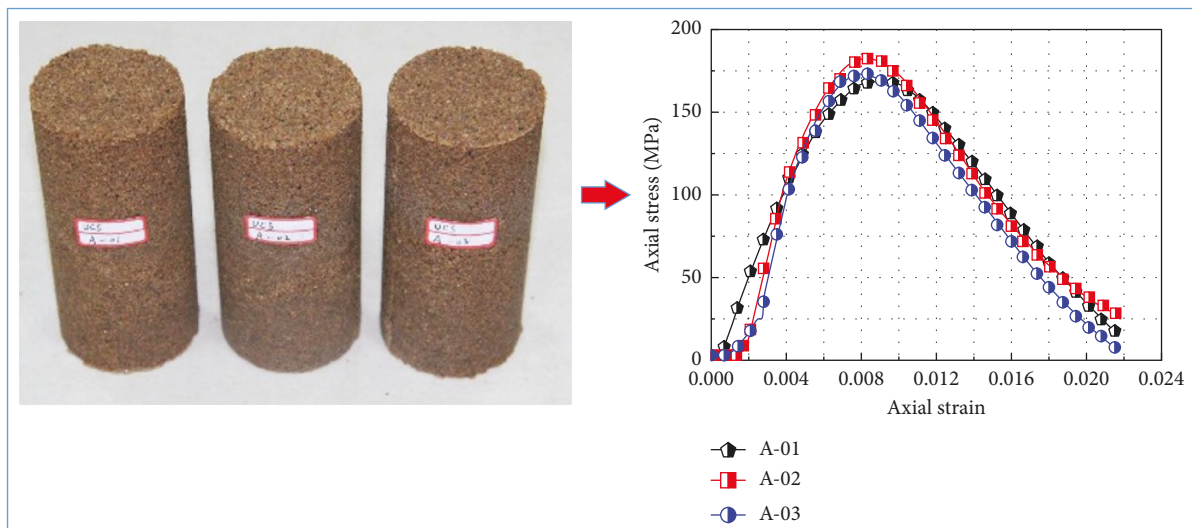


FIGURE 3: Standard samples and stress-strain curve.

TABLE 1: Uniaxial compression test results.

Mass ratio (sand: paraffin: Hydraulic oil)	Sample number	Height (mm)	Diameter (mm)	Mass (g)	Density/(kg/m ³)	UCS (kPa)
1500:100:100	A-1	103.18	50.42	374.69	1819.7	169.06
	A-2	103.62	50.94	383.9	1818.8	182.91
	A-3	103.04	51.58	383.0	1779.7	173.65
	Average	103.28	50.98	380.53	1806.67	175.21

TABLE 2: Similar material ratios for different layers of similar material models.

Rock stratum number	Lithology	Original layer thickness/(m)	Model thickness/(mm)	Matching number	Material proportioning and dosage (consider 30% loss/kg)					Laying thickness (mm)
					Sand	Calcium carbonate	Plaster	Water	Total	
R-26	Clay	4.4	29.33	9:7:3						
R-25	Coarse sand	1	6.67	9:5:5	81.08	4.50	4.50	9.01	99.10	35
R-24	Clay	5.5	36.67	9:7:3	81.08	6.31	2.70	9.01	99.10	35
R-23	Coarse sand	4.1	27.33	9:5:5	69.50	3.86	3.86	7.72	84.94	30
R-22	Loam	2.5	16.67	9:6:4	34.75	2.32	1.54	3.86	42.47	15
R-21	Coarse sand	17.5	116.67	9:5:5	277.99	15.44	15.44	30.89	339.77	120
R-20	Clay	6	40.00	9:7:3	92.66	7.21	3.09	10.30	113.26	40
R-19	Coarse sand	2.4	16.00	9:5:5	34.75	1.93	1.93	3.86	42.47	15
R-18	Clay	3.2	21.33	9:7:3	46.33	3.60	1.54	5.15	56.63	20
R-17	Coarse sand	19	126.67	9:5:5	289.58	16.09	16.09	32.18	353.93	125
R-16	Clay	9.4	62.67	9:7:3	139.00	10.81	4.63	15.44	169.88	60
R-15	Coarse sand	2.1	14.00	9:5:5	34.75	1.93	1.93	3.86	42.47	15
R-14	Loam	9.5	63.33	9:6:4	139.00	9.27	6.18	15.44	169.88	60
R-13	Siltstone	8.9	59.33	7:5:5	144.14	10.30	10.30	16.47	181.21	60
R-12	Fine grained sandstone	1.2	8.00	7:8:2	264.26	26.43	11.33	30.20	332.22	110
R-11	Medium grained sandstone	15.4	102.67	7:7:3						
R-10	Mudstone	6.2	41.33	8:6:4	91.52	6.86	4.58	10.30	113.26	40
R-9	Medium grained sandstone	2.2	14.67	7:7:3	36.04	3.60	1.54	4.12	45.30	15
R-8	Mudstone	1.5	10.00	8:6:4	60.06	6.86	1.72	6.86	75.50	25
R-7	Fine grained sandstone	2	13.33	7:8:2						
R-6	Siltstone	1.7	11.33	7:5:5	57.20	4.29	2.86	6.44	70.79	25
R-5	Mudstone	2.2	14.67	8:6:4						
R-4	Siltstone	7.4	49.33	7:5:5	120.12	8.58	8.58	13.73	151.01	50
R-3	Fine grained sandstone	5.44	36.27	7:8:2	84.08	9.61	2.40	9.61	105.71	35
R-2	Medium grained sandstone	2.4	16.00	7:7:3	48.05	4.80	2.06	5.49	60.40	20
R-1	Siltstone	8.47	56.47	7:5:5	132.13	9.44	9.44	15.10	166.11	55
C*	3 coal loading	6	40.00	9:6:4	83.40	5.56	3.71	9.27	101.93	40
F-01	Mudstone	3.33	22.20	8:6:4	45.76	3.43	2.29	5.15	56.63	20
F-02	Siltstone	6.6	44.00	7:5:5	108.11	7.72	7.72	12.36	135.91	45
F-03	Medium grained sandstone	38.67	257.80	7:7:3	624.62	62.46	26.77	71.39	785.24	260
Total					3219.96	253.22	158.73	363.19	3995.11	1370

mining face is slightly higher than that of other working faces. The first reason is that the internal humidity of the model is uneven, the humidity of the first mining face is high, and the roof strength is low and the other reason is that

the two sides of the model are not well shielded and supported before and after the mining of simulated working face. As a result, the model is greatly affected by the simulated mining operation.



FIGURE 4: Temperature-controlled strips in a similar material model.

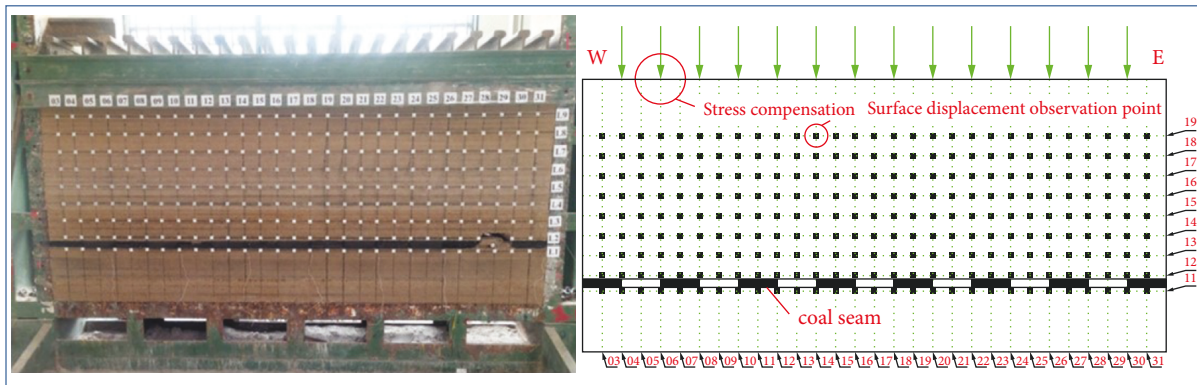


FIGURE 5: Surface displacement monitoring points.

The total station is used to observe the surface measuring points of the working face before and after mining, and the vertical displacement increments of overlying strata before and after mining are analyzed and compared by selecting L1, L2, L3, L5, and L8 measuring lines. The position of the L1–L5 horizontal measuring lines are shown in Figure 7. When working faces are not mined, all the measuring points on each measuring line are located in the same horizontal position. After mining the strip working face from right to left in turn, the observation results are shown in Figures 8–12.

Figure 8 shows that the displacement of the L3 measuring line changes with the mining of the working face. With the mining of the working face, the roof of the coal pillar adjacent to the working face obviously sinks, and the roof of the coal pillar far away from the mining face is not sensitive to the influence of mining. Affected by the mining on both sides of the working face, the strip pillar roof generally has two large subsidence, and the first subsidence is greater. Because only one side of the coal pillar at the boundary of the mining area is affected by the mining face, the roof subsidence is less than that of the strip coal pillar.

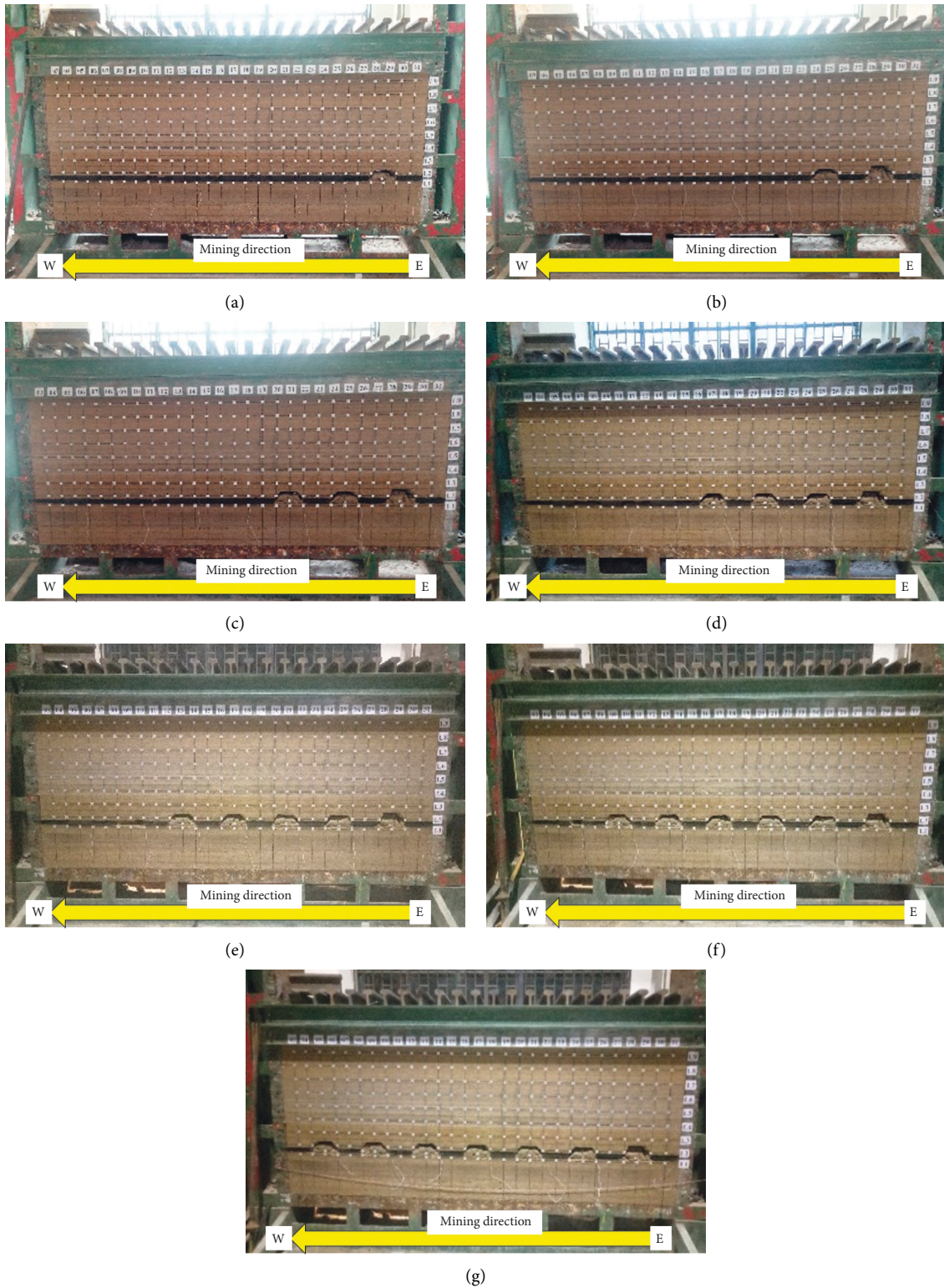


FIGURE 6: Process of sequential mining of strip working face. (a) 1# working face, (b) 2# working face, (c) 3# working face, (d) 4# working face, (e) 5# working face, (f) 6# working face, and (g) 7# working face.

Figure 9 shows the observation results of each measuring point on the L1 measuring line. The L1 measuring line is located on the floor of the coal seam. After the strip working face is mined, the overlying load originally acting on the coal

seam of the working face begins to transfer to the periphery and the load on the coal pillar increases. At the same time, the coal pillar can also be used as a stress transfer medium to transfer the increased load to the coal seam floor. Under this



FIGURE 7: Position of L1-L5.

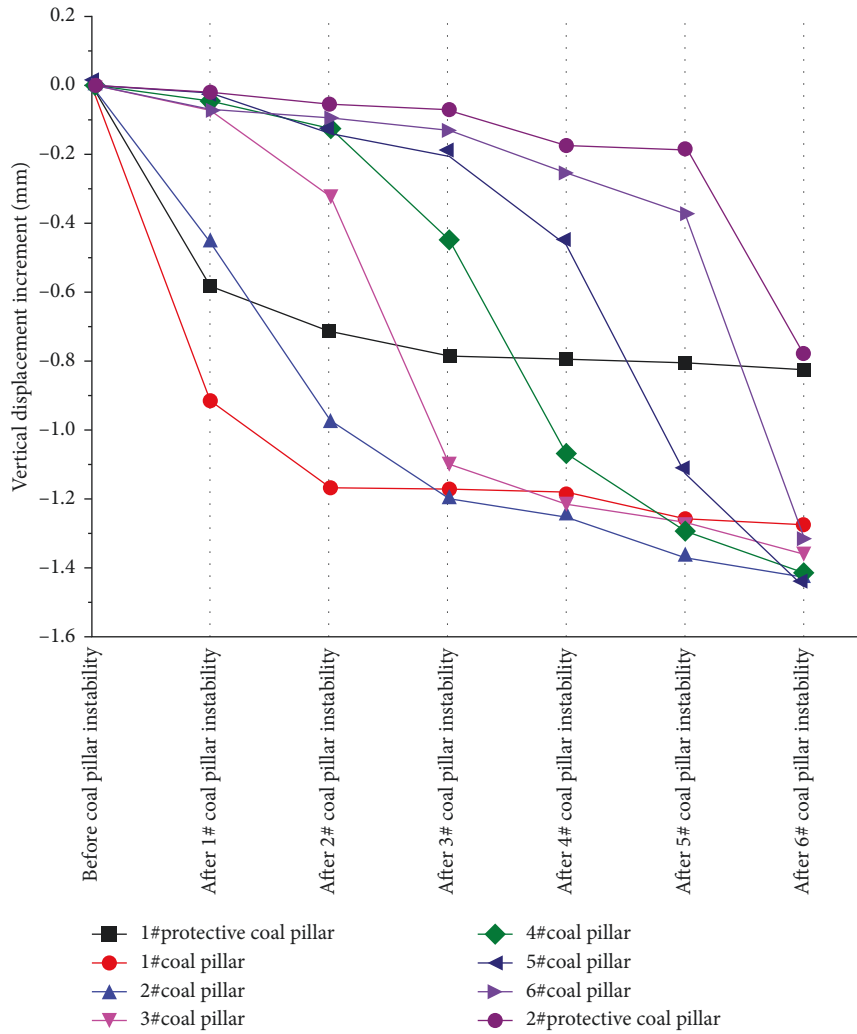


FIGURE 8: Vertical displacement of measuring point above the coal pillar online L3.

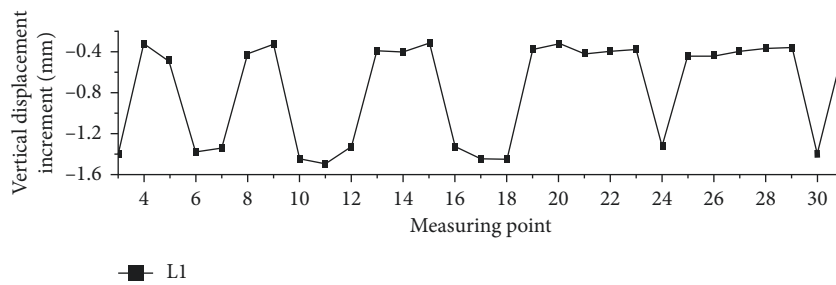


FIGURE 9: Vertical displacement observation of line L1.

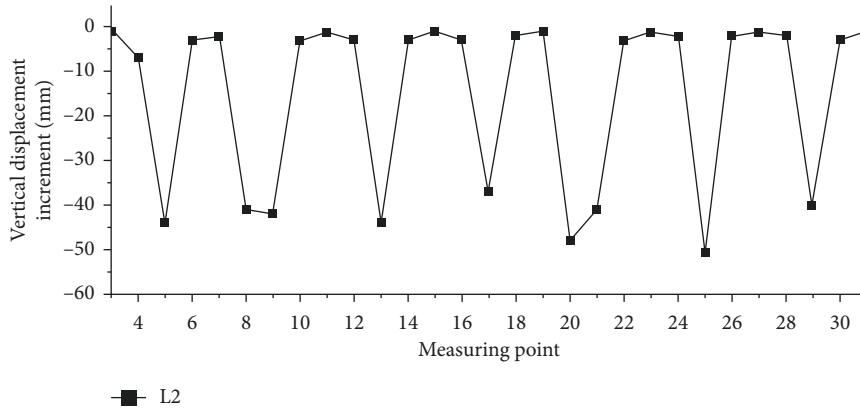


FIGURE 10: Observation results of vertical displacement of line L2.

influence, the coal pillar floor produces the maximum vertical compression deformation of 1.5 mm. In addition, the observation results show that the compression deformation position of the floor is not completely corresponding to the position of the coal pillar, indicating that the transfer of load of the coal pillar to the overlying rock is not uniform, and there is a high stress area in the floor under high load, the rock mass moves to both sides or lower strata under stress, while the rock mass in the low stress area may have deformation characteristics such as compression, bulging, and subsidence.

Figure 10 shows the observation results of the L2 line, and the measuring points located in the upper part of the goaf all decrease with the fall of the rock strata. The subsidence of the measuring point above each goaf is between 37 and 51 mm, with average subsidence of 43.1 mm. The reason why the average subsidence of the measuring point is greater than the mining height of the coal seam is that the pin at the measuring point is loose and slips under the impact of roof caving. The measuring point at the junction of goaf and coal pillar also has 1–6 mm subsidence, which is due to the loss of lateral restraint at the edge of coal pillar after mining, resulting in plastic failure under a load of the roof, resulting in vertical compression deformation.

Figure 11 shows the observation results of the L3 and L5 monitoring lines. Due to the collapse of the direct roof, the upper strata of the goaf are bent and deformed, and cracks appear in some positions. The subsidence of the L3 measuring line in the upper part of goaf is 4.01–5.1 mm. The subsidence of measuring points in the upper part of the coal pillar is in the range of 2.07–3.04 mm, and the subsidence of this part of measuring points superimposes the compression of the coal pillar and the strata. The L5 measuring line as a whole shows the shape of low in the middle and high at both ends. The corresponding relationship between the subsidence of each measuring point and the position of the coal pillar and goaf is not obvious, indicating that the uneven subsidence of the roof caused by mining in the working face is not effectively transmitted upward. The reason is that a thick hard rock layer at the L5 measuring line maintains a good self-supporting capacity after mining. The bending deformation occurs only due to the overall compression and subsidence of the coal pillar.

Figure 12 shows the observation results of the L8 monitoring line and the subsidence shape is similar to that of the L5 monitoring line. Because the rock stratum of the L5 monitoring line blocks the upward development of uneven subsidence below, and because the lithology of the rock stratum at L8 is weaker than that at the L5 monitoring line, the deformation characteristics of the rock stratum at the L8 monitoring line are controlled by the rock stratum at L5, so there is a subsidence form similar to that of L5 monitoring line.

3.2. Coal Pillar Instability Stage. In order to simulate the failure and instability stage of strip coal pillar, the strip coal pillar is heated step by step. The heating voltage is set at 50 V, 75 V, 100 V, 110 V, 120 V, and 130 V, respectively, and the heating duration of each stage is 24 h. During the heating process, the rock stratum displacement at the L3 measuring line of the strip coal pillar roof is observed. The displacement increment under different electric pressures is shown in Figure 13.

In order to facilitate data processing and analysis, the measuring points are divided into four types according to the location: the measuring points on the upper part of the protective coal pillar, the measuring points on the edge of the strip coal pillar, the measuring points on the upper part of goaf and the measuring points on the upper part of strip coal pillar. The displacement of each type of measuring point under each voltage level is taken as the average value. When the step heating voltage rises from 50 V to 100 V, the displacement of each measuring point is in the range of 1–2.14 mm, which is caused by the rise of temperature in the coal pillar and the softening of paraffin near the electric heating wire, but the coal pillar remains stable as a whole at this time. When the voltage rises to 110 V, each measuring point only slightly sinks on the original foundation, and the coal pillar remains stable, and no instability occurs. When the voltage increases from 110 V to 130 V, the displacement of each measuring point increases rapidly. Except for the upper part of the protective coal pillar, the average subsidence of the other areas exceeds 4 mm, and the upper subsidence of the strip coal pillar is 3.5 mm. The

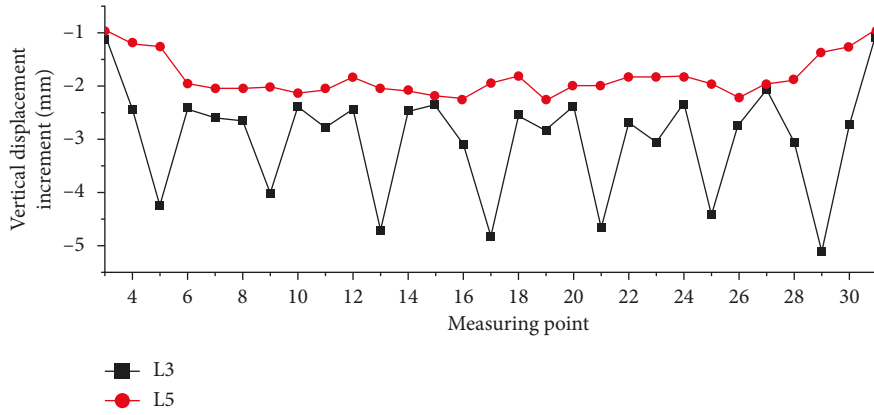


FIGURE 11: Observation results of vertical displacement of line L3 and line L5.

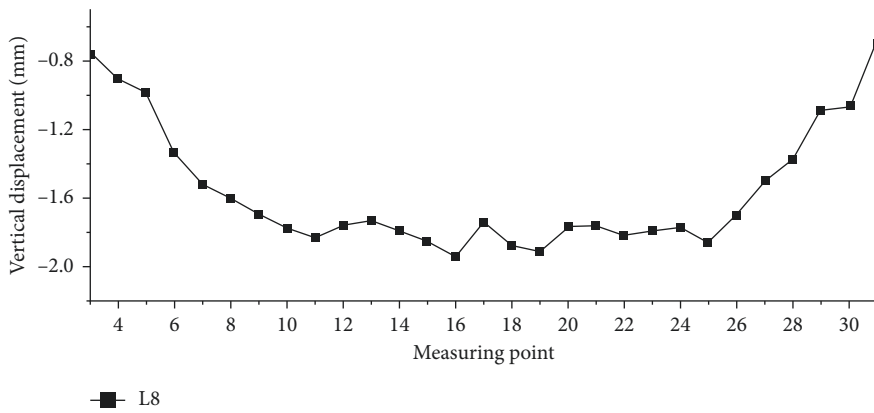


FIGURE 12: Vertical displacement observation of line L8.

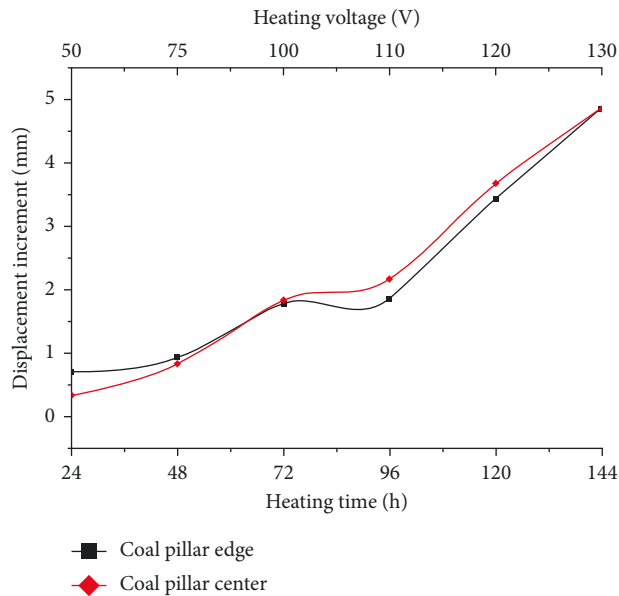


FIGURE 13: Average vertical displacement of the upper pillar line of L3 when heating by classification.

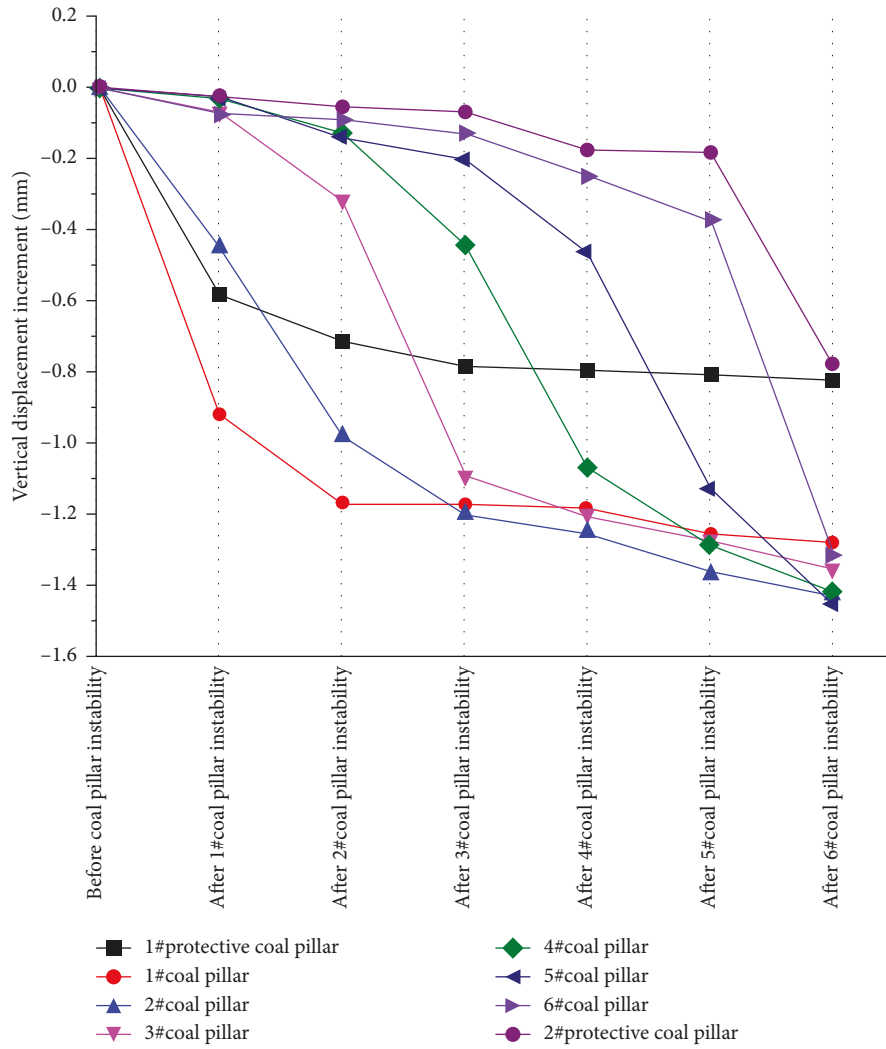


FIGURE 14: Displacement of measuring points above the coal pillars online L3 after the instability of coal pillars.

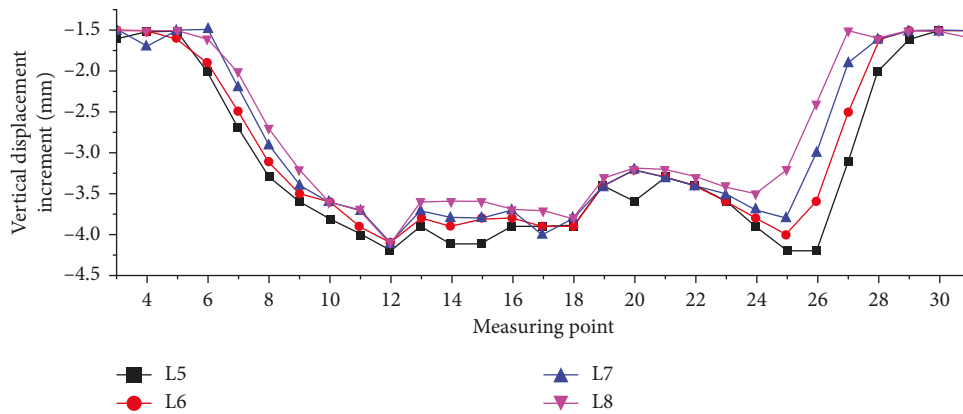


FIGURE 15: Vertical displacement of line L5–L8 after instability of coal pillar.

observation results show that all the paraffin in the coal pillar has been softened, so it is judged that the coal pillar has been unstable.

In order to facilitate the analysis, the subsidence of the coal pillar before instability is zeroed. Figure 14 is the displacement change law of measuring points above the coal

pillar on the L3 measuring line after the strip coal pillar is unstable.

After the strip coal pillar is unstable, it produces compression deformation due to plastic failure. After the roof rock layer is superimposed with the compression deformation of the coal pillar, the vertical displacement increases accordingly. Compared with that before the instability of strip coal pillar, the average subsidence of the coal pillar roof increases by 93%, and the maximum subsidence of the roof occurs when the lower coal pillar is unstable. Similar to the mining of strip working face, the protective coal pillar at the mining area boundary is stable due to the influence of mining on only one side, and its roof subsidence is significantly less than that of the strip coal pillar, which mainly comes from the elastic deformation caused by the increase of vertical stress.

Figure 15 shows the vertical displacement of the L5–L8 measuring lines after all the strip coal pillars in the mining area are unstable. The model sinks as a whole, and the minimum subsidence is 1.5 mm. The average subsidence of four monitoring lines decreases gradually from bottom to top because with the decrease of buried depth, the influence of overburden stress transfer caused by mining and coal pillar instability on shallow strata decreases gradually. At the same time, because there is no separation layer in the model, the subsidence shape of each side line is basically the same. There are two uplifts of the four measuring lines in the middle of the mining area, which is larger than the fluctuation value of the L5 measuring line before the instability of the coal pillar. The reason is that the instability of the strip coal pillar leads to periodic fracture of the key layer in the overlying rock and the torsion of the rock beam.

4. Conclusion

- (1) The strip coal pillar model made by the ratio of river sand: paraffin: hydraulic oil = 1500:100:100 is uniform and stable, and the strength discreteness is small. In addition, the instability process of the strip coal pillar is simulated successfully by using the method of embedding an electric heating wire in the model.
- (2) After strip coal pillar mining, the roof caving of each working face is basically the same, and the development of fracture zone and bending zone is not obvious. The rock strata where the L5 monitoring line is located controls the movement of overlying strata up to the surface, and its subsidence shape as a whole appears as a “disk” with a gradual transition from high at both ends to low in the middle, and the subsidence coefficient is about 94% lower than that of the working face of longwall mining under the same geological conditions.
- (3) Affected by the load transfer of the overlying strata in the goaf after mining, the maximum subsidence of the L5 monitoring line above the strip coal pillar is 2.2 mm, and the maximum subsidence of the strip coal pillar after instability is 4.2 mm. The subsidence shape of the upper monitoring line changes from “disk” to “basin.”
- (4) The instability of strip coal pillar will lead to significant and more harmful overburden movement between overburden and surface than that of strip working face. Finally, the movement and deformation characteristics of overburden and surface are similar to those of full mining. Because the coal pillar after instability still has a certain bearing capacity, the maximum subsidence of the surface is still far less than that under the condition of longwall mining.

Data Availability

The data used to support the findings of this study are available from the corresponding author upon request.

Conflicts of Interest

The authors declare that there are no conflicts of interest regarding the publication of this paper.

Acknowledgments

This research was financially supported by National Natural Science Foundation of China (51904167).

References

- [1] F. M. Li, “Current status and development tendency of coal mining subsidence area treatment technology in China,” *Coal mining technology*, vol. 3, pp. 8–10, 2011.
- [2] S. J. Chen, H. L. Wang, H. Y. Wang, G. Weijia, and L. Xiushan, “Strip coal pillar design based on estimated surface subsidence in eastern China,” *Rock Mechanics and Rock Engineering*, vol. 49, no. 9, pp. 3829–3838, 2016.
- [3] W. Gao and M. M. Ge, “Stability of a coal pillar for strip mining based on an elastic-plastic analysis,” *International Journal of Rock Mechanics and Mining Sciences*, vol. 87, pp. 23–28, 2016.
- [4] W. B. Zhu, S. C. Yu, D. Y. Xuan, Z. Shan, and J. Xu, “Experimental study on excavating strip coal pillars using caving zone backfill technology,” *Arabian Journal of Geosciences*, vol. 11, no. 18, 2018.
- [5] Z. C. Qin, W. Nie, Y. L. Liu, Y. B. Zhang, and L. N. Liu, “Location selection of lower layer mining roadway in thick coal seam bifurcation area,” *Journal of Shandong University of Science and Technology*, vol. 39, no. 3, pp. 43–49, 2020.
- [6] W. B. Guo, K. Z. Deng, and Y. F. Zou, “Research status and main issues of strip mining in China,” *Coal Science and Technology*, vol. 32, no. 8, pp. 7–11, 2004.
- [7] X. J. Zhu, G. L. Guo, and H. Yang, “Surface subsidence prediction method of backfill-strip mining in coal mining,” *Bulletin of Engineering Geology and the Environment*, vol. 78, no. 8, pp. 6235–6248, 2019.
- [8] X. J. Zhu, F. Zha, G. L. Guo, and X. Yang, “Surface subsidence prediction method of backfill-strip mining in coal mining,” *Advances in Civil Engineering*, vol. 78, 2021.
- [9] W. B. Guo, Q. L. Hou, and Y. F. Zou, “Relationship between surface subsidence factor and mining depth of strip pillar mining,” *Transactions of Nonferrous Metals Society of China*, vol. 21, pp. S594–S598, 2012.
- [10] T. B. Zhao, S. Q. Ma, and Z. Y. Zhang, “Ground control monitoring in backfilled strip mining under the metropolitan

- district: case study,” *International Journal of Geomechanics*, vol. 18, no. 7, 2018.
- [11] J. J. Snodgrass and D. A. Newman, “In situ technique for the assessment of failure in coal pillars,” in *Proceedings of the 26th U S Symposium On Rock Mechanics*, pp. 1181–1188, USA, January 1985.
- [12] A. W. Kahir and S. S. Peng, “Causes and mechanisms of massive pillar failure in a southern West Virginia coal mine,” *Mining Engineering*, vol. 37, no. 4, pp. 323–328, 1985.
- [13] P. H. Lu, “Triaxial-loading measurement for mine-pillar stability evaluation,” in *Proceedings of the 27th U S Symposium On Rock Mechanics*, pp. 379–385, Tuscaloosa, Alabama, June 1986.
- [14] M. D. G. Salamon and A. H. Munro, “A study of the strength of coal pillars,” *Journal of the South African Institute of Mining and Metallurgy*, vol. 68, no. 2, pp. 56–67, 1967.
- [15] B. N. Hu, “Stability analysis of coal pillar in strip mining,” *Journal of China Coal Society*, vol. 20, no. 2, pp. 205–210, 1995.
- [16] H. P. Xie, F. B. Duan, and H. W. Zhou, “Research Progress on stability theory and analysis method of strip coal pillar,” *China Mining Magazine*, vol. 5, pp. 37–41, 1998.
- [17] X. M. Cui and X. X. Miu, “Study on stress analysis and subsidence curve shape in strip coal pillar,” *Journal of China University of Mining and Technology*, vol. 4, pp. 52–55, 2000.
- [18] W. Gao, “Elastic-plastic analysis of stability of inclined coal pillar,” *Mechanics in Engineering*, vol. 2, pp. 23–26, 2001.
- [19] W. B. Guo, K. Z. Deng, and Y. F. Zou, “Cusp Catastrophic Model of Instability of strip coal pillar along strike,” *Chinese Journal of Rock Mechanics and Engineering*, vol. 23, no. 12, pp. 1996–2000, 2004.
- [20] Y. J. Yang, N. N. Zhao, D. P. Ma, and F. J. Zhang, “Study on stability of strip coal pillar with different moisture content,” *Journal of Mining and Safety Engineering*, vol. 33, no. 1, pp. 42–48, 2016.
- [21] S. J. Chen, *Basic Experimental Study on Long-Term Stability of Deep Strip Coal Pillar*, Shandong University of Science and Technology, China, 2009.
- [22] W. Guo, H. Wang, and S. Chen, “Coal pillar safety and surface deformation characteristics of wide strip pillar mining in deep mine,” *Arabian Journal of Geosciences*, vol. 92, pp. 1–9, 2016.
- [23] D. J. Xue, “Determination of uniaxial compressive strength of intact rock,” *Journal of Shandong University of Science and Technology*, vol. 39, no. 4, pp. 28–36, 2020.
- [24] X. Qu, S. J. Chen, D. W. Yin, and S. Liu, “Experimental study of the strip coal pillar models failure with different roof and floor conditions,” *Archives of Mining Sciences*, vol. 66, no. 3, pp. 475–490, 2021.
- [25] Y. Tan, H. Xu, W. T. Yan et al., “Study on the overburden failure law of high-intensity mining in gully areas with exposed bedrock,” *Frontiers of Earth Science*, vol. 10, 2022.
- [26] Y. Tan, H. Cheng, and S. Gong, “Field study on the law of surface subsidence in the high-intensity fully mechanized caving mining working face with shallow thick bedrock and thin epipedon in hilly areas,” *Advances in Materials Science and Engineering*, vol. 2021, Article ID 6515245, 2021.
- [27] L. Y. Liu, W. C. Ma, and W. D. Wang, “Dual damage mechanism of supercritical CO₂ adsorption induced weakening effect on coal,” *Journal of Shandong University of Science and Technology*, vol. 39, no. 4, pp. 79–86, 2020.
- [28] Y. Q. Su, F. Q. Gong, S. Luo, and Z. X. Liu, “Experimental study on energy storage and dissipation characteristics of granite under two-dimensional compression with constant confining pressure,” *Journal of Central South University*, vol. 28, no. 3, pp. 848–865, 2021.
- [29] M. Z. Gao, B. G. Yang, J. Xie et al., “The Mechanism of Microwave Rock Breaking and its Potential Application to Rock-Breaking Technology in Drilling,” *Petroleum Science*, vol. 19, 2022.
- [30] Q. Wang, S. Xu, Z. X. Xin, H. Wei, and B. Jiang, “Mechanical properties and field application of constant resistance energy-absorbing anchor cable,” *Tunnelling and Underground Space Technology*, vol. 125, 2022.
- [31] C. Zhu, M. Karakus, M. C. He et al., “Volumetric deformation and damage evolution of Tibet interbedded skarn under multistage constant-amplitude-cyclic loading,” *International Journal of Rock Mechanics and Mining Sciences*, vol. 152, 2022.
- [32] F. X. Li, D. W. Yin, F. Wang, Jiang, and Li, “Effects of combination mode on mechanical properties of bi-material samples consisting of rock and coal,” *Journal of Materials Research and Technology*, vol. 19, pp. 2156–2170, 2022.
- [33] Z. G. Tao, Q. Geng, C. Zhu et al., “The mechanical mechanisms of large-scale toppling failure for counter-inclined rock slopes,” *Journal of Geophysics and Engineering*, vol. 16, no. 3, pp. 541–558, 2019.
- [34] Y. Wang, H. N. Yang, J. Q. Han, and C. Zhu, “Effect of rock bridge length on fracture and damage modelling in granite containing hole and fissures under cyclic uniaxial increasing-amplitude decreasing-frequency (CUIADF) loads,” *International Journal of Fatigue*, vol. 158, 2022.
- [35] G. Li, Y. Hu, S. M. Tian, M. Weibin, and H. L. Huang, “Analysis of deformation control mechanism of prestressed anchor on jointed soft rock in large cross-section tunnel,” *Bulletin of Engineering Geology and the Environment*, vol. 80, no. 12, pp. 9089–9103, 2021.